Rise and fall of void population governs the porous-to-solid transition in soft granular materials

Jyoti Sonawane[1,*], Srinivas Selvaraju[1,*], Priyanka Nayar[2], Prashant K. Purohit[3], and Shailendra P. Joshi[1,†]

[1]Department of Mechanical and Aerospace Engineering, University of Houston, TX 77204, USA
[2]The Kinkaid School, 201 Kinkaid School Drive Houston, TX 77024
[3]Department of Mechanical Engineering and Applied Mechanics, University of Pennsylvania, PA 19104, USA

April 23, 2026

Abstract

Soft granular materials are porous packings of highly deformable particles found in systems ranging from blood clots and tissue scaffolds to starchy foods and 3D-printing inks. They start as collections of discrete, loosely packed motifs, but then transition to a coherent solid under load. Understanding when that *granular-to-continuum* transition occurs is critical because it controls whether a biomaterial can be injected through a needle, how easily cells and drugs infiltrate a healing wound, and how nutrients are transported through engineered tissue. Classical approaches rely on counting inter-particle contacts, but this becomes rather ambiguous as contact points evolve into contact surfaces when soft grains undergo large, nonlinear changes in size and shape. Here, we present a paradigm shift: instead of tracking the granular material, we track the empty space between them. Through computational simulations, we discover that porosity evolves through a universal sequence: as the material compresses, interstitial voids undergo a stereotyped cascade of fragmentation (proliferation) followed by collapse (elimination). We identify a topological marker that marks the exact onset of solid-like rigidity and stress homogenization. The critical threshold of this topological marker is independent of the particle size distribution or elasticity, offering a robust geometry-based descriptor for the solidification of soft matter.

*These authors contributed equally
†Corresponding author: shailendra@uh.edu

1 Introduction

Soft granular materials (SGMs) are scientifically challenging (Jaeger et al., 1996; Weaire and Aste, 2008; Manning, 2023), technologically stimulating (Follmer et al., 2012), and often therapeutic (Widener et al., 2024; Yuk et al., 2021). They occur in natural systems, ranging from food materials (Karathanos and Saravacos, 1993; Huang and Clayton, 1990) to wound healing (Angelini et al., 2011; Griffin et al., 2015; Bosek et al., 2022), and are emerging as mechanical motifs for tissue repair (Riley et al., 2019) and cell delivery (Qazi and Burdick, 2021; Cai, 2023), in soft robotics (Manti et al., 2016; Li et al., 2024), and biofabrication (Daly, 2024). Their intrinsic disorder and modularity combined with deformability offer pathways to endow them with trainability (Jaeger et al., 2024).

In classical granular materials with elastically stiff grains, the structure–property relation is typified by packing fraction (ψ) and the mean coordination number ($\langle Z \rangle$, average number of contacts per grain). By contrast, the nonlinear grain-scale deformability of SGMs introduces complexities in how particles transmit forces in ways that are distinct from their stiff counterparts (Brodu et al., 2015; Emiroglu et al., 2022; Verheyen et al., 2023). As contacts broaden into finite regions (Mason et al., 1995; Brodu et al., 2015), faceting occurs and force chains delocalize. In such situations, the notion of $\langle Z \rangle$ may become mechanically ambiguous (Mukhopadhyay and Peixinho, 2011). Indeed, recent work on highly deformable granular architectures (Poincloux and Takeuchi, 2024) highlights that rigidity transitions (Damavandi et al., 2022a,b) can be governed by geometric measures such as the extent of the contacts rather than the number of contacts. These observations suggest that, in the post-jamming regime relevant to many SGMs, structure–property relations should be formulated in terms of geometric variables that remain well defined under large deformation (Vu et al., 2019; Vu and Barés, 2019).

This motivates a fundamental mechanistic question: *when does a compacting SGM behave as a granular assembly versus as a continuum solid?* This crossover, which may be viewed as the onset of a rigidity transition, is mechanistically relevant because it marks the transition from force-chain-dominated stress transmission to a regime in which the stress field becomes nearly homogeneous on the sample scale, making a continuum description appropriate. Consequently, the evolution of the interstitial porosity that leads these architectures to a *confluent* (i.e., space-filling) state can have implications for healing and rupture (Prakash et al., 2021; Varner et al., 2023). SGM densification reorganizes the void network, which can have functional implications, for example, on the stability and health of biological SGMs (Monfared et al., 2023), in transport (Tutwiler et al., 2018; Truong et al., 2019; Bhattacharjee and Datta, 2019; Qazi and Burdick, 2021; Bhattacharjee et al., 2021), and in modulating texture of starchy foods (Huang and Clayton, 1990; Rahman, 2001)), see Fig. 1.

In this work, we show that for densifying SGMs driven toward confluence from an initially jammed yet porous state, the void population (number of distinct interstitial voids) provides a robust microstructural marker of the granular-to-continuum crossover. Using finite-element simulations of two-dimensional assemblies of compressible hyperelastic grains, we find that densification generically drives a two-stage evolution of the void network: fragmentation (void proliferation) followed by void evanescence as confluence is approached. The void population peaks at a threshold packing fraction that is essentially independent of grain compressibility and particle-size distribution, and this threshold coincides with

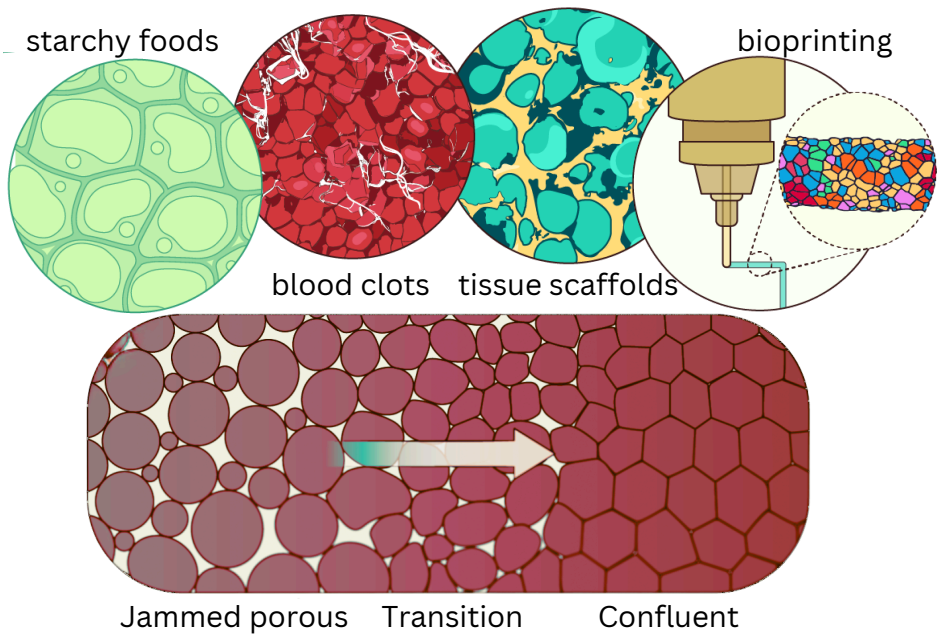

Figure 1 Exemplars of confluent granular motifs (top). In these and similar applications, soft granular aggregates go through a transition from a jammed to a confluent state (bottom) under mechanical forces, which determines their functional behaviors.

a crossover in the macroscopic force–displacement response and with the onset of stress homogenization. This identifies a confluence-associated rigidity crossover in SGMs that is more naturally associated with the void-space topology rather than by coordination. This aspect, combined with the evolution of associated void statistics (distributions of void area, aspect ratios, and orientations), provides richer information for void-scale mechanics that complements contact-mechanics-based design and is naturally compatible with data-driven materials pipelines informed by experiments (Verheyen et al., 2023; Tateno et al., 2025) and simulations.

2 Approach

We simulate the compaction behavior of SGMs under uniaxial loading. Three types of particle size distributions (PSDs) with kinematic periodicity are considered: uniform (u-PSD), wide Gaussian (wG-PSD), and narrow Gaussian (nG-PSD). The nG-PSD resembles a nominally monodisperse system. To keep computations tractable, we posit statistical volume elements (SVEs) that are representative of the parent granular assembly for each PSD and consider multiple realizations (N_{sve}) of such SVEs, see Fig. A1; the procedure for constructing SVEs is discussed in Appendix A. Table 1 collates the information relevant to the SVEs for each PSD.

A typical initial SGM architecture (Fig. 2) comprises loosely packed, stress-free assembly of grains. We use ABAQUS/STANDARD® as the finite element solver to conduct numerical simulations. Figure 2 shows an illustrative example of an SVE comprising 80 particles meshed using approximately 543,000 plane strain (CPE8H) finite elements. Each particle is assumed to follow a compressible neo-Hookean

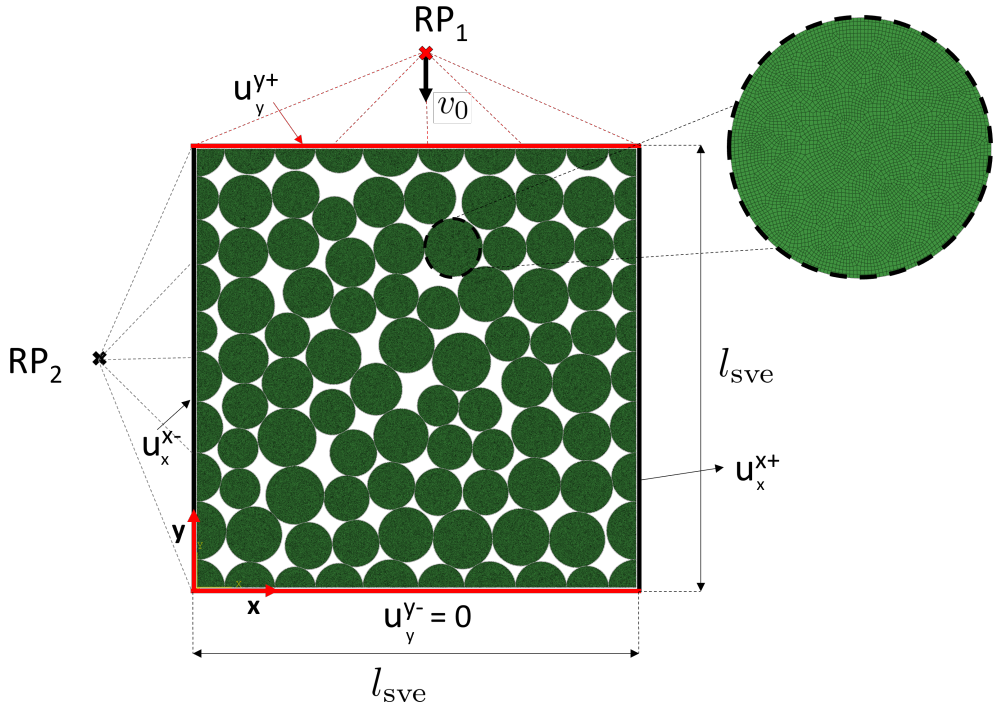

Figure 2 An illustrative SVE with the finite element mesh. Kinematic periodic boundary conditions are prescribed at the reference nodes R_{p1} and R_{p2}. Typical particle with fine finite element mesh is shown in the enlarged view.

constitutive response described by the strain energy density function (Holzapfel, 2002; Vu et al., 2021):

$$\mathcal{W} = \frac{E}{2(1+\nu)}\left(\frac{I_1 - 3}{2} - \ln J + \frac{\nu}{1-2\nu}(\ln J)^2\right) \tag{1}$$

where $I_1 = \mathrm{tr}(\mathbf{F}^\mathsf{T}\mathbf{F})$, and $J = \det(\mathbf{F})$ with $\mathbf{F}$ being the deformation gradient. We take the modulus $E = 0.45$ MPa and consider three different levels of particle compressibility ranging from nearly incompressible ($\nu = 0.495$) to moderately compressible ($\nu = 0.34$) and highly compressible ($\nu = 0.20$).

As indicated in Fig. 2, the SVE edges follow kinematic periodic boundary conditions that are en-

Table 1 Summary of particle assemblies considered in this work. N_{sve} = number of realizations per PSD; $\langle N_p \rangle$ = average number of particles per realization, l_{sve} = SVE size, r_{mean} = mean particle radius per realization, and $\langle \psi_0 \rangle$ = average initial packing fraction per realization. SD = one standard deviation.

PSD	N_{sve}	l_{sve} (mm)	$\langle N_p \rangle$	$\langle r_{mean} \rangle \pm$ SD (mm)	$\langle \psi_0 \rangle \pm$ SD
Uniform	6	110	80	6.19 ± 0.75	0.8076 ± 0.0034
*w*G	10	50	31	4.09 ± 0.46	0.8082 ± 0.0053
*n*G	25	50	25	5.01 ± 0.35	0.7908 ± 0.0029

forced using multipoint constraint equations:

$$u_j^{\mathrm{i}+} - u_j^{\mathrm{i}-} = \epsilon_{ij}^0 L_i^0, \quad \text{no sum on } i \tag{2}$$

where u_j is the displacement in direction j ($= \mathrm{x}, \mathrm{y}$), ϵ_{ij}^0 is the applied (nominal) strain on the SVE, and $L_i^0 \equiv l_{\mathrm{sve}}$ is the initial dimension in the i^{th} direction. The system is compressed by applying a constant velocity (v_0) at $\mathrm{R_{p1}}$ along the y direction. The bottom edge ($\mathrm{y} = 0$) is constrained by prescribing $u_{\mathrm{y}}^{\mathrm{y}-} = 0$. The macroscopic state of strain is uniaxial by virtue of setting $\epsilon_{\mathrm{xx}}^0 = 0$ (that is, $u_{\mathrm{x}}^{\mathrm{x}-} = u_{\mathrm{x}}^{\mathrm{x}+}$) at $\mathrm{R_{p2}}$. The inter-particle contact conditions are modeled using a surface-to-surface contact formulation within ABAQUS/STANDARD®. Tangential contact is modeled with a Coulomb friction formulation with a friction coefficient $\mu = 0.2$, while the normal contact behavior is enforced using the default hard-contact formulation to prevent mesh penetration.

3 Results

The following normalized quantities are defined to describe the macroscopic state of a granular system: $|\bar{\sigma}| \equiv \langle \sigma_{\mathrm{yy}} \rangle / E^*$ where $\langle \sigma_{\mathrm{yy}} \rangle = A_{\mathrm{sve}}^{-1} \int \sigma_{\mathrm{yy}} \, \mathrm{d}A_{\mathrm{p}}$ is the average normal stress in the loading (y) direction, $E^* = E/(1-\nu^2)$ is the effective modulus; $\bar{\Delta} \equiv \Delta / l_{\mathrm{sve}}$ where $\Delta = v_0 t$ is the compressive displacement applied by prescribing a nominal velocity v_0 and l_{sve} the initial dimension of an SVE, and $\psi \equiv A_{\mathrm{p}}/A_{\mathrm{sve}}$ is the current packing fraction in terms of the current total area of the particles (A_{p}) and the current area of the SVE (A_{sve}). In what follows, we primarily discuss the results for *u*-PSD and refer to the trends from *w*G- and *n*G-PSD simulations in the context. Detailed results for *w*G- and *n*G-PSDs are summarized in Appendix B.

3.1 Micromechanical Landscape

Fig. 3 shows how the stress distribution evolves in a typical granular assembly with *u*-PSD for the three compressibility cases. In the early stages ($\psi \sim 0.87$, first column), the characteristic force-chain motifs are clearly seen and are qualitatively similar in all three cases. With increasing compaction ($\psi \sim 0.94$, second column), there is still a semblance of a force-chain network in all three cases, although it is significantly diffuse. At an even later stage ($\psi \sim 0.97$, third column), the force chains are no longer evident and replaced by localized regions of stress heterogeneity surrounding the residual voids. Subtle differences emerge in the force-chain motifs as the particle contacts develop in a manner that depends on the particle compressibility. In the range $0.94 \lesssim \psi \lesssim 0.97$, faceted particle clusters emerge with relatively uniform stress, while force chains vanish. At $\psi \sim 1$ (fourth column), force chains disappear and the assembly resembles a homogeneously stressed bulk solid. In a fully packed state, the more compressible granular assemblies show more laterally elongated particles, and their SVE boundaries are more wavy compared to their less compressible counterparts. These observations suggest that subtle differences in the diffuse force-chain networks and the related porosity characteristics manifest strongly in the final deformed packing state, as discussed next.

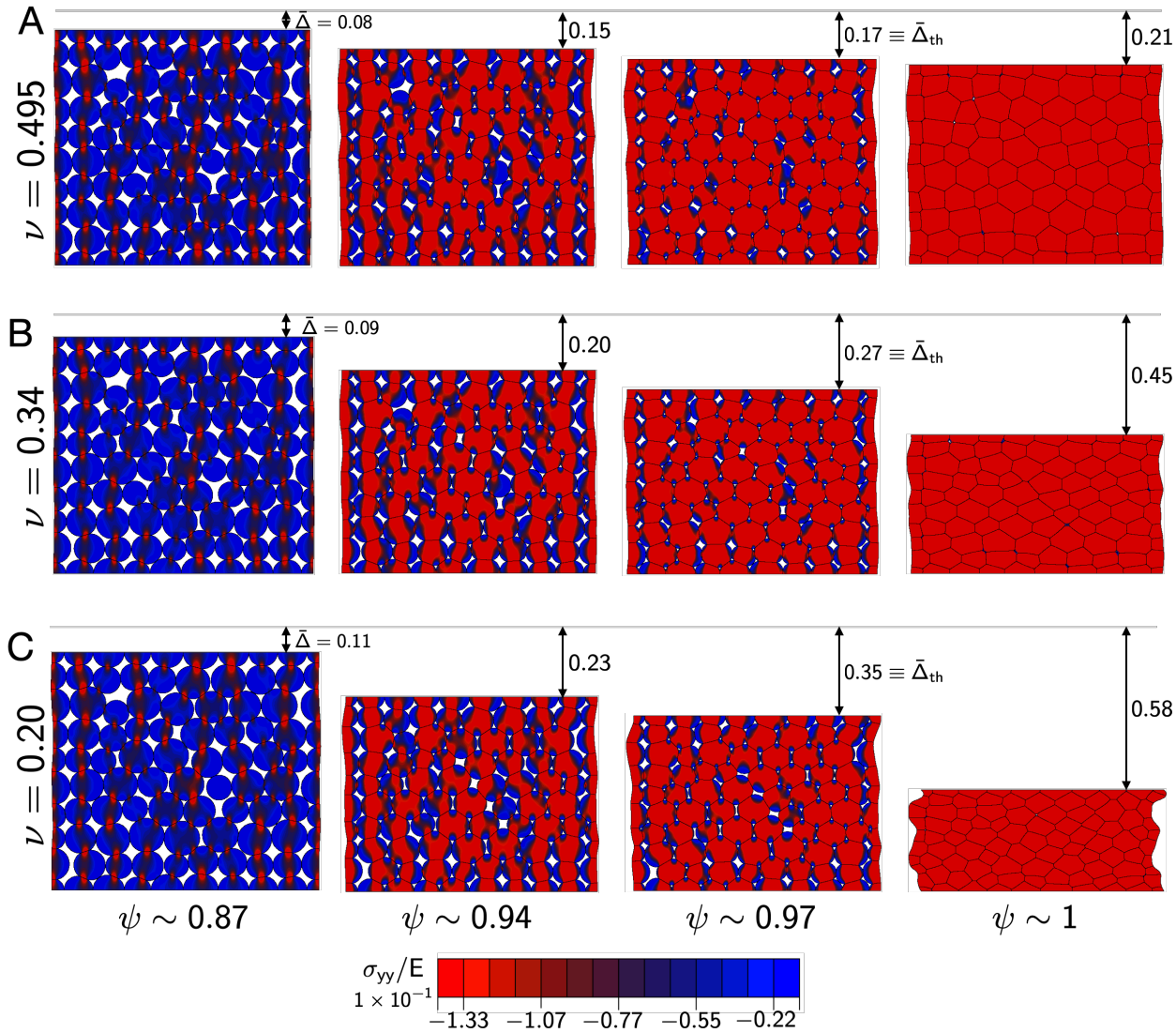

Figure 3 Deformed profiles of a typical granular assembly (u-PSD) showing the normalized stress (σ_{yy}/E) motifs for (A) $\nu = 0.495$, (B) $\nu = 0.34$, and (C) $\nu = 0.2$. $\bar{\Delta}_{th}$ is a threshold displacement (Eq. (14)). Other PSDs show similar trends (Fig. B1).

Fig. 4a shows the evolution of the normalized void population (N_v/N_v^0) with packing fraction (ψ), where N_v is the total number of voids at a given ψ and N_v^0 the initial void population in a microstructure. For each compressibility level, three PSDs are shown: uniform (u), wide Gaussian (wG), and narrow Gaussian (nG). For reference, the results for square packing are included, which serve as the a limiting case for nominally monodisperse systems.

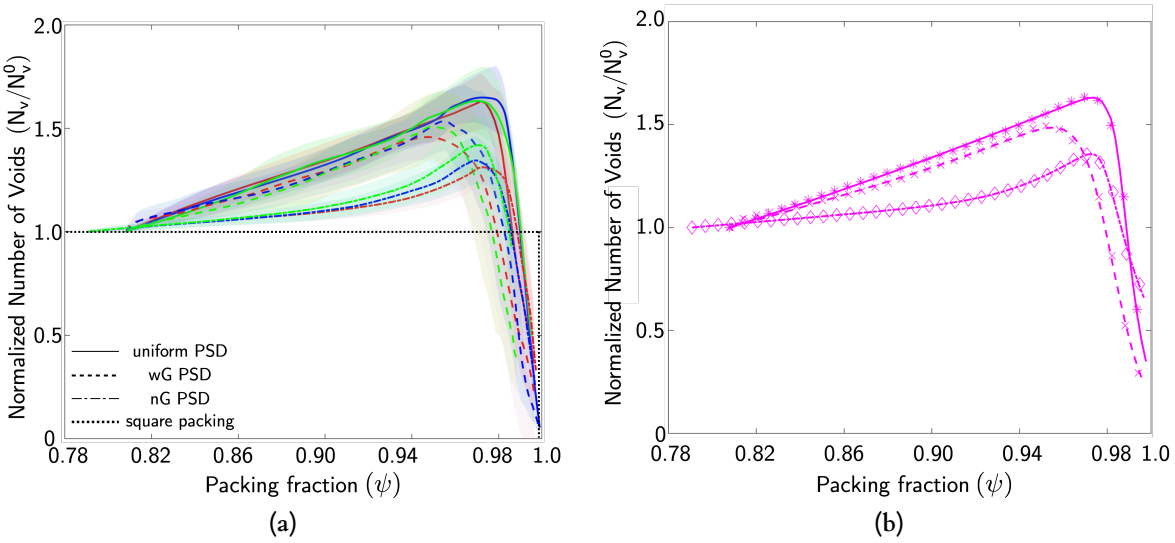

Figure 4 Evolution of the total number of voids (N_v) normalized by the initial number of voids (N_v^0) with packing fraction (ψ). (a) Finite element simulation results shown for $\nu = 0.495$ (red), $\nu = 0.34$ (blue), and $\nu = 0.20$ (green). Shaded regions indicate one standard deviation. For reference, evolution for a regular square packing is also shown. Panel (b) shows the comparison of the results from the proposed birth-death model (Eq. (12), solid lines) with the finite element results (symbols) for the three PSDs.

For the three particle compressibilities, a common trend is observed for the three PSDs: N_v first increases, reaches a peak, $(N_v)^{\text{peak}}$, corresponding to a threshold packing fraction ψ_{th}, and then decreases rather rapidly. Remarkably, for all three PSDs and ν cases, the void population reaches a peak at $0.95 \lesssim \psi_{\text{th}} \lesssim 0.98$. We also find that at this stage of packing (i.e., $\bar{\psi}_{\text{th}} \sim 0.97$), the variance of the particle stresses is negligible, $\text{Var}(|\bar{\sigma}|) \sim 0.035$, which implies that the granular assemblies are more or less homogeneously stressed. Thus, the ψ at which coexistence of granular and continuum regions is observed more or less coincides with that at which the stress in the entire granular assembly is uniform.

The increase in the number of voids under compressive loading is intriguing. Unlike tensile loading of bulk solids where voids may nucleate (Gent and Lindley, 1959; Hang-Sheng and Abeyaratne, 1992; Noell et al., 2023; Barney et al., 2020; Lefèvre et al., 2015), here the increase in void population is not due to void nucleation but rather to the fragmentation of existing voids. A closer look at the deformed granular assemblies (Fig. 3, Fig. B1) reveals that packing evolution is facilitated by two mechanisms: (i) breaking up of voids due to particle contact (void fragmentation) and (ii) deformation-induced decrease in the area of individual voids (void shrinkage).

For a given ν, u-PSD shows the fastest increase to peak followed by wG-PSD, with nG-PSD exhibiting the slowest increase. In the ideal case of perfectly square arrangement of mono-sized particles,

the rate of increase is zero because all voids shrink at the same rate and vanish together without undergoing a fragmentation process. In other words, the closer a PSD is to being monodisperse, the slower the void population increases and the lower the peak void population. A characteristic feature is observed in the case of *n*G-PSD. Although its void population increases slowly relative to the other two PSDs, it shows a brief but perceptible surge just before reaching $(N_v)^{\text{peak}}$. The initial sluggish increase correlates with it being less disordered than the *u*-PSD and *w*G-PSD counterparts (although their initial porosities are in the same range). In that sense, its population growth is closer to the square-packing case in that the voids tend to preferentially shrink rather than fragment. However, once the voids have sufficiently shrunk, these architectures undergo rapid fragmentation leading to an increase in the rate of N_v just before reaching the peak. This late surge in fragmentation clearly separates *n*G-PSD from an ideal mono-sized regular square packing. Moreover, for $\nu = 0.2$, the particles tend to undergo significant lateral deformation (see Fig. 3C at $0.97 \lesssim \psi \lesssim 1$), further increasing the rate of N_v.

To understand the relative roles of fragmentation and shrinkage in this transition, we propose a model motivated by population dynamics.

From a geometric standpoint, the total area of interstitial voids in a granular assembly at a given ψ is $A_v(\psi) = N_v(\psi)\, a_v(\psi)$ where N_v is the current total number of voids, A_v the current total voided area, and a_v the current average area per void. Under compressive loading, $A_v(\psi)$ and $a_v(\psi)$ both decrease monotonically with ψ. Defining the following normalized rates $\tilde{N}_v(\psi) := \dot{N}_v/N_v$, $\tilde{A}_v(\psi) := -\left|\dot{A}_v/A_v\right|$ and $\tilde{a}_v(\psi) := -\left|\dot{a}_v/a_v\right|$ where $\dot{(\ )} \equiv \partial(\ )/\partial\psi$, we obtain:

$$\tilde{N}_v(\psi) = \tilde{A}_v(\psi) - \tilde{a}_v(\psi) \tag{3}$$

Eq. (3) gives a kinematic relation between the fractional rates of change of the void population, the total void area, and the mean void area of an individual void.

Numerical simulations (Fig. 4) motivate a kinetic model that mimics population dynamics in mathematical biology (Murray, 2007):

$$\tilde{N}_v(\psi) = r(\psi)\left(1 - \frac{N_v}{K(\psi)}\right) - m(\psi) \tag{4}$$

where $r(\psi)$ and $m(\psi)$ are, respectively, the effective rates of *birth* (fragmentation) and *death* (evanescence), and $K(\psi)$ is an effective capacity.

To connect $K(\psi)$ to the void statistics measured in the simulations, we introduce a characteristic void area $a_{\min}$ that defines the smallest size that is counted as a distinct void. Voids smaller than $a_{\min}$ are screened. A precise definition may depend on the functional consequence. For instance, from a mechanical behavior standpoint, $a_{\min}$ can be the mean void area at the transition ψ_{th}, where the stress field transitions to becoming nearly homogeneous, and further fragmentation is effectively stalled. On another note, solely from a numerical or experimental standpoint, $a_{\min}$ could reflect a void below the resolution of interest. If the total area of the voids $A_v(\psi)$ was divided into voids of size $a_{\min}$, the maximum corresponding number of distinguishable voids would be $K(\psi) = A_v(\psi)/a_{\min}$. Substituting

this into Eq. (4) yields (with $A_v = N_v a_v$)

$$\tilde{N}_v(\psi) = r(\psi)\left(1 - \frac{a_{\min}}{a_v(\psi)}\right) - m(\psi) \tag{5}$$

Relating Eq. (3) and Eq. (5), we interpret $r(\psi)$ and $m(\psi)$ as controlling, respectively, the reduction in mean void area due to fragmentation and the reduction in the overall voided area. That is:

$$\tilde{a}_v(\psi) = -\, r(\psi)\left(1 - \frac{a_{\min}}{a_v(\psi)}\right); \qquad \tilde{A}_v(\psi) = -\, m(\psi) \tag{6}$$

where $r(\psi) \geqslant 0$ and $a_v > a_{\min}$.

With $N_v^0 = N_v(\psi_0)$ and $a_v^0 = a_v(\psi_0)$, integrating Eq. (5) yields

$$\frac{N_v(\psi)}{N_v^0} = \frac{a_v^0 e^{-M(\psi)}}{a_{\min} + (a_v^0 - a_{\min})e^{-R(\psi)}} \tag{7}$$

where

$$R(\psi) := \int_{\psi_0}^{\psi} r(s)\, ds, \qquad M(\psi) := \int_{\psi_0}^{\psi} m(s)\, ds \tag{8}$$

Guided by the numerical trends (Fig. 4), we prescribe

$$r(\psi) = r_{\text{pre}} + \Delta r\, s(\Psi_r), \qquad m(\psi) = m_{\text{pre}} + \Delta m\, s(\Psi_m) \tag{9}$$

where $\Delta r = r_{\text{post}} - r_{\text{pre}}$, $\Delta m = m_{\text{post}} - m_{\text{pre}}$, and the logistic switch

$$s(\Psi) := \frac{1}{1 + e^{-k\Psi}}, \qquad \Psi_r = \frac{\psi - \psi_{\text{r}}}{w_r}, \qquad \Psi_m = \frac{\psi - \psi_{\text{m}}}{w_m} \tag{10}$$

where ψ_{r} and ψ_{m} control the packing fraction at which N_v peaks, i.e., ψ_{th}; $r_{\text{pre}}, m_{\text{pre}}$ and $r_{\text{post}}, m_{\text{post}}$ are the pre- and post-peak levels, and w_r, w_m set the transition widths. With these choices, the cumulative rates $R(\psi)$ and $M(\psi)$ are obtained in closed form as

$$R(\psi) = r_{\text{pre}}\Delta\psi + \mathcal{S}_{\text{r}}\Delta r, \qquad M(\psi) = m_{\text{pre}}\Delta\psi + \mathcal{S}_{\text{m}}\Delta m \tag{11}$$

where $\Delta\psi = \psi - \psi_0$ with ψ_0 being the initial packing fraction. Further, $\mathcal{S}_\beta = \frac{w_\beta}{k} \ln\left(\frac{1+e^{k\Psi_\beta}}{1+e^{k\Psi_\beta^0}}\right)$ with $\Psi_\beta^0 = (\psi_0 - \psi_\beta)/w_\beta$ for $\beta \in \{r, m\}$.

Substituting Eq. (11) into Eq. (7) yields an explicit closed-form expression for $N_v(\psi)/N_v^0$ in terms of the model parameters $\{r_{\text{pre}}, r_{\text{post}}, m_{\text{pre}}, m_{\text{post}}, k, w_r, w_m, \psi_{\text{r}}, \psi_{\text{m}}, a_{\min}, a_v^0\}$, which can be written in a compact form as:

$$\frac{N_v(\psi)}{N_v^0} = \frac{e^{\gamma(\psi)}}{\eta} \tag{12}$$

where $\gamma(\psi) = R(\psi) - M(\psi)$, and $\eta = 1 + \kappa(e^{R(\psi)} - 1)$ with $\kappa = a_{\min}/a_v^0$. $\gamma(\psi)$ quantifies the

balance between the fragmentation ($R(\psi)$) and shrinkage ($M(\psi)$) driven mechanisms. When $\gamma > 0$, the fragmentation process dominates, causing the void population to increase. In the shrinkage-dominated regime, $\gamma < 0$, causing the void population to decay. Consequently, the rigidity transition corresponds to $\gamma = 0$. The term η term serves as a constraint on exponential evolution.

Fig. 4b plots Eq. (12) using the parameters in Table 2. Note that ψ_{th} and N_v^{peak}/N_v^0 are obtained as outputs. Based on these trends, the trends in Fig. 4 can be summarized as follows. The near-overlap of *u*-PSD and *w*G-PSD indicates that their fragmentation and shrinkage stay nearly the same over most of the loading path. As such, their curves differ mainly by how strongly γ is biased negative on the approach to the crossover. By contrast, the sluggish early growth in *n*G-PSD implies that shrinkage competes effectively with fragmentation. Its brief pre-peak surge is the signature of a localized acceleration in $R(\psi)$ that temporarily drives γ positive just before the crossover. In other words, in *n*G-PSD voids preferentially shrink rather than fragment for most of the loading path; however, once they have sufficiently shrunk, they rapidly fragment, thereby producing the late sharp rise before reaching the peak.

Table 2 Summary of calibrated parameters in Eq. (12) for the three cases in Fig. 4b. a_v^0 is obtained from the actual SVEs and $a_{\min} = 0.05$ is kept fixed.

PSD	ψ_r	ψ_m	w_r	w_m	k	r_{pre}	r_{post}	m_{pre}	m_{post}	a_v^0
Uniform (*u*)	0.98	0.99	0.001	0.12	41.3	5.1	18.0	0.85	139.4	0.29
Wide Gaussian (*w*G)	0.95	0.98	0.31	0.07	10.3	5.74	12.12	1.0	114.4	0.15
Narrow Gaussian (*n*G)	0.94	0.98	0.76	0.12	47.8	1.2	7.82	0.04	45.5	0.22

3.2 Macroscopic Responses

Fig. 5a shows the evolution of the packing fraction (ψ), which can be described by (Selvaraju et al., 2024)

$$\psi = \mathcal{P}\,\psi_0 \tag{13}$$

where ψ_0 is the initial packing fraction and $\mathcal{P} = (1 - |\epsilon_{\text{p}}|)/(1 - |\bar{\Delta}|) \equiv (1 - \alpha|\bar{\Delta}|^n)/(1 - |\bar{\Delta}|)$, with α and n as fitting parameters (Table 3) relating ϵ_{p} to $\bar{\Delta}$ (inset in Fig. 5a), where $|\epsilon_{\text{p}}| = \sum_{i=1}^{N_{\text{p}}}(A_{\text{p}}^i/A_{\text{p0}}^i) - 1$ is the magnitude of the total areal strain of N_{p} particles in an SVE; A_{p}^i is the current area of particle i and A_{p0}^i its initial area. This strain partition coefficient, $\mathcal{P}$, denotes the fraction of imposed deformation that is effective in reducing porosity as opposed to being accommodated by particle area change. In a granular assembly comprising nearly incompressible particles ($\nu = 0.495$), the area change resulting from the applied deformation must be accommodated entirely by porosity reduction. In other words, $|\epsilon_{\text{p}}|$ is negligible ($\alpha \ll 1$ and $n \approx 1$); therefore, $\psi \approx \psi_0/(1 - \bar{\Delta})$. By contrast, in a system of compressible particles, the overall area change results from a combination of particle area change and porosity reduction. Consequently, for the same $\bar{\Delta}$, porosity reduction is smaller in these cases compared to its incompressible counterpart, and therefore the packing fraction evolves slowly. Comparing the evolution profiles of ψ and ϵ_{p} (Fig. 5a) indicates that between these two processes accommodating the applied

deformation, porosity reduction governs in the early stages while particle area change takes over at later stages.

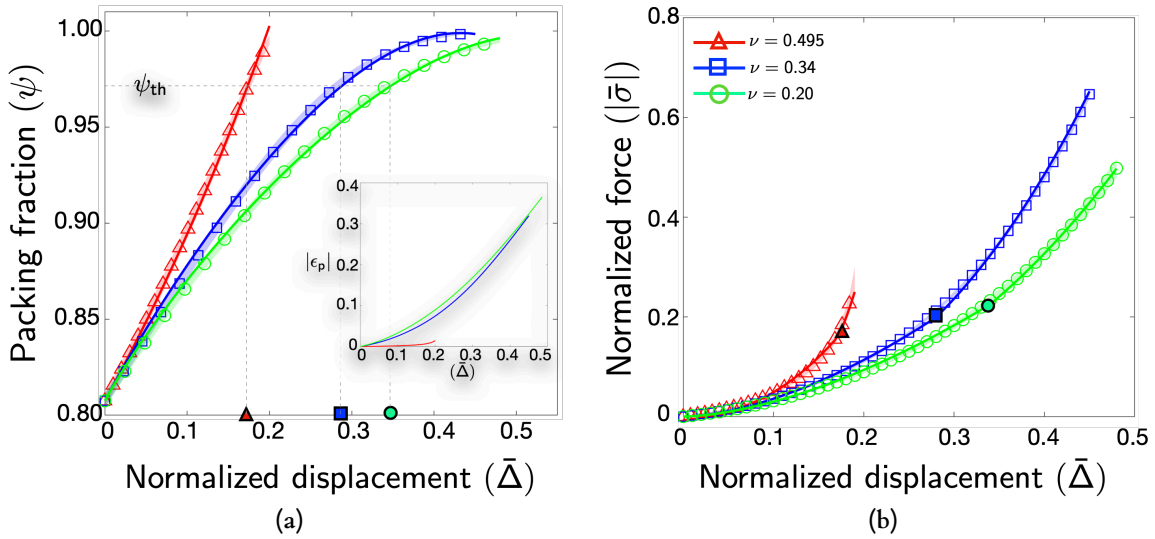

Figure 5 Evolution of (a) overall packing fraction (ψ) and (b) normalized overall force ($|\bar{\sigma}|$) with normalized applied deformation ($\bar{\Delta}$). Open symbols: finite element results averaged over N_{sve} realizations. Shaded regions: one standard deviation. Solid lines: analytical fits (Eq. (13) and Eq. (14)). Filled symbols denote $\bar{\Delta}_{th}$ corresponding to $\bar{\psi}_{th}$. The inset in Panel (a) shows the magnitude of the total particle areal strain ($|\epsilon_p|$). Results are shown for uniform PSD. Other PSDs show similar trends (Fig. B2).

Fig. 5b shows the corresponding normalized stress evolution for three cases of particle compressibility. With decreasing particle compressibility (ν), stress stiffening occurs earlier for the same average initial packing fraction (ψ_0). Using regression, we find that the $|\bar{\sigma}| - \bar{\Delta}$ response is best captured by a two-stage power-law fit:

$$|\bar{\sigma}| = \begin{cases} S_0\, \bar{\Delta}^{\beta_0}, & \text{if } \bar{\Delta} \leqslant \bar{\Delta}_{th} \\ S_1\, \bar{\Delta}^{\beta_1}, & \text{if } \bar{\Delta} > \bar{\Delta}_{th} \end{cases} \tag{14}$$

where $\bar{\Delta}_{th}$ is the threshold normalized displacement that corresponds to $\bar{\psi}_{th}$ (Fig. 5a). In other words, the occurrence of the peak in the void population also marks a transition in the macroscopic stiffening of SGMs. Table 3 collates the parameters fitted to u-PSD. These parameters are fitted for individual SVE datasets using the fmincon function in MATLAB®. The parameters for other PSDs are given in the Appendix B (Table B1, B2). As seen, the higher the particle compressibility, the more delayed the transition.

Table 3 Calibrated values for parameters in Eq. (13) and Eq. (14) (mean ± SD) for u-PSD. Table B1 and B2 collate values for uG-PSD and nG-PSD, respectively.

ν	α	n	$\bar{\Delta}_{th}$	S_0	β_0	S_1	β_1
0.495	0.035 ± 0.003	1.020 ± 0.0002	0.173 ± 0.004	7.86 ± 0.27	2.21 ± 0.02	405.74 ± 35.84	4.45 ± 0.002
0.34	1.35 ± 0.02	1.80 ± 0.02	0.28 ± 0.0002	1.93 ± 0.02	1.76 ± 0.004	4.49 ± 0.05	2.42 ± 0.01
0.20	1.14 ± 0.02	1.58 ± 0.03	0.339 ± 0.0003	1.34 ± 0.07	1.65 ± 0.04	2.69 ± 0.09	2.29 ± 0.01

3.3 Void Statistics

The probability density functions (PDFs) in Fig. 6 (also see Fig. B3 and Fig. B4 in Appendix B) reveal that, for a given PSD, SGMs follow a geometric pathway of void evolution under compression that is agnostic to material compressibility. The PDFs of the normalized void area (Fig. 6a–6c) exhibit a bimodal character that indicates two families of void sizes. With increasing packing, the PDF trends persist, but shift to the left. A closer look at Fig. 3 suggests that the two families could be elongated four-sided voids and smaller three-sided voids that also form by fragmentation of the four-sided voids as the grains come into contact. As the length of the contact line between adjacent grains increases, the area of the three-sided voids decreases.

The PDFs of the aspect ratio of the void (Fig. B3) also shift to the left with increasing packing, indicating the progressive disappearance of elongated voids; yet, the overall structure of the slope remains very similar at different particle compressibilities. In contrast, void orientations (Fig. B4) show very little change with packing and show no significant dependence on particle compressibility. This suggests that rearrangements occur through particle shape evolution rather than rotational reorganization of voids.

4 Discussion

Although void connectivity and void geometry have been quantified under SGM compaction (Vu and Barés, 2019; Tateno et al., 2025), the void population itself has not been identified as a mechanistic marker of the onset of confluence. In this work, we show that as the packing evolves, the void population exhibits a robust signature across PSDs, independent of particle compressibility: (i) proliferation via void fragmentation, leading to (ii) the occurrence of a peak void population, followed by (iii) rapid void evanescence as the system approaches fully dense packing. Particle compressibility amplifies the geometric contrast between ordered and disordered packings. The rate at which an SGM system approaches the onset of confluence depends on both geometric and mechanical parameters, but is nearly independent of the threshold packing fraction (ψ_{th}). Decreasing particle compressibility and increasing initial granular disorder accelerate void proliferation, that is, confluence appears at a smaller threshold deformation ($\bar{\Delta}_{\mathrm{th}}$). This creates a mechanical fingerprint in the macroscopic force–displacement response that transitions from one power-law regime to another at $\bar{\Delta}_{\mathrm{th}}$.

These geometric and mechanical aspects of SGM compaction can have important implications in various applications. In granular hydrogels, a packing-fraction-controlled jamming/yield point marks the transition from flowable microgel suspensions to mechanically coherent, load-bearing networks, with concomitant changes in injectability and yield behavior (Riley et al., 2019; Qazi and Burdick, 2021; Emiroglu et al., 2022). In bioprinting or slurry-based processes, the relative position of $\bar{\Delta}_{\mathrm{th}}$ along the force–displacement curve provides a natural indicator of when a material transitions from easily flowing to mechanically load-bearing. In biological analogs such as blood clots, which are composed

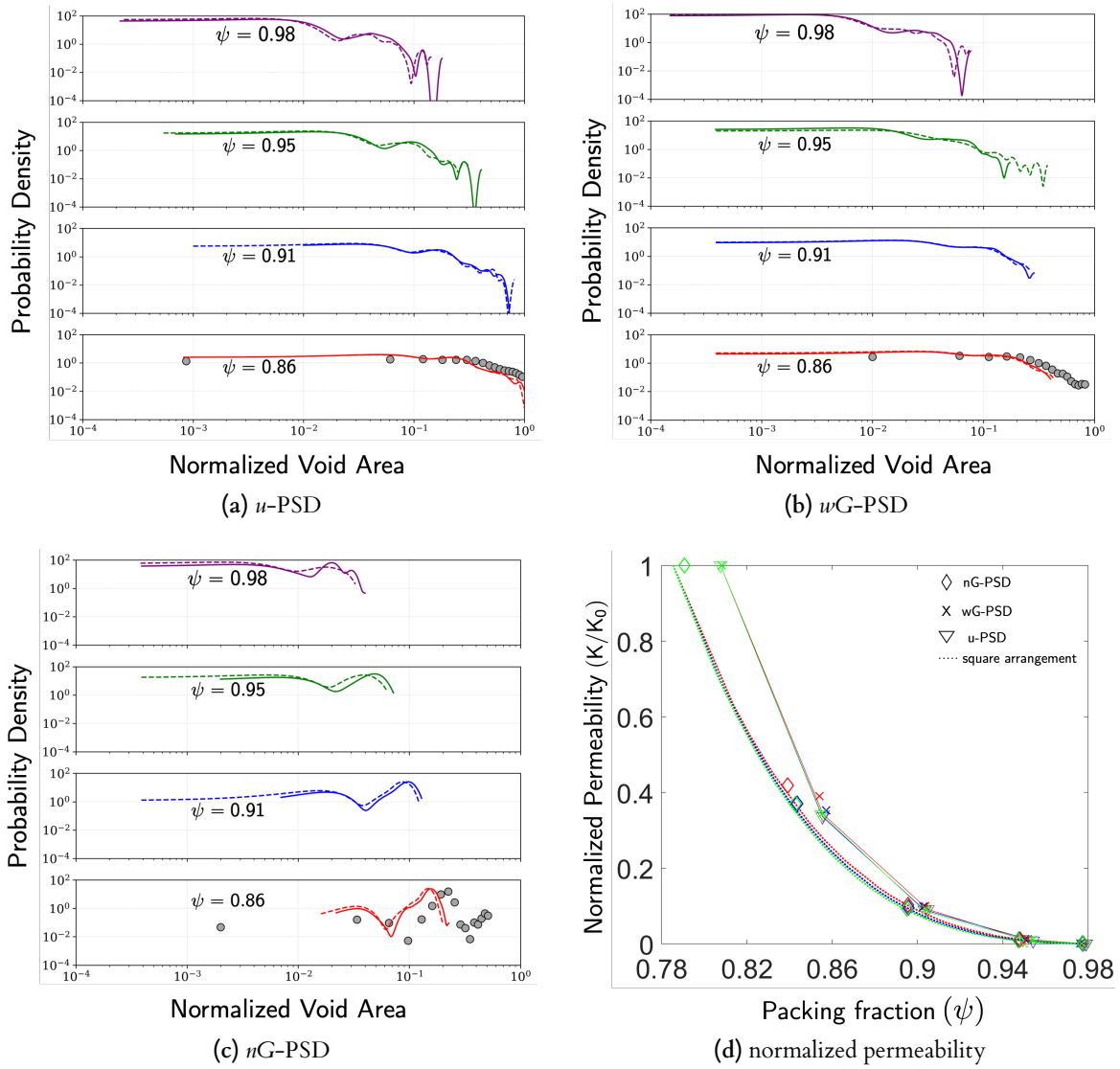

Figure 6 (a-c) Evolution of the averaged (over SVEs) probability density functions of the normalized void area per void with packing fraction (ψ) illustrated for $\nu = 0.495$ (solid lines) and $\nu = 0.2$ (dashed lines). Circles indicate the distributions at initial packing fraction (ψ_0). Panel (d) shows the evolution of the normalized permeability with packing fraction (cf. Eq. (15)) for $\nu = 0.495$ (red) and 0.2 (green); solid lines show the trend for u-PSD and dashed lines for the square arrangement; K_0 is the permeability at ψ_0.

largely of red blood cell (RBC) aggregates in their core, this threshold can be interpreted as the onset of confluence, the point at which a clot becomes mechanically coherent while still deformable (Varner et al., 2023; Tutwiler et al., 2018; Peshkova et al., 2025). Our analysis predicts the manner in which particle size distribution, elasticity, and initial volume fraction of such systems must have an effect on the stress at which void fragmentation occurs, and therefore on the reduction of the rate of clot degradation due to clot contraction. Voids could also become sites of nucleation of cracks in clots; therefore, the reduction in void size due to contraction reduces the size of flaws and should lead to an increase in the loads required for crack advance (Tutwiler et al., 2020; Varner et al., 2023). It has been shown that the shapes of RBCs in contracted clots play an important role in hemostasis. They are polyhedral with faces that tend to be triangles, quadrilaterals, pentagons, and hexagons (Tutwiler et al., 2018). These shapes are seen in our results, particularly in near-incompressible particles (cf. Fig. 3 and Fig. B1).

Beyond the mechanics of rigidity transition, the statistics of void population can be important in quantifying other properties. For example, in flow through porous media (Hommel et al., 2018), evolving void structures play a role in permeability. In porous cereals and bread-like food foams, densification under compressive loads results in the rapid evolution of the void structure, which is closely related to their texture and transport (Van Dalen et al., 2007; Gao et al., 2018). In blood clots, contraction is caused by platelets and osmotic depletion interactions of RBCs (Peshkova et al., 2025). It has been observed that the rate of clot degradation by fibrinolytic enzymes slows as contraction increases (Risman et al., 2022). Thus, changes in the permeability and recanalization pathways may be correlated with the void population. While a detailed analysis of porosity-transport relation is beyond the scope of this work, the foregoing results can be used in permeability evolution with packing fraction as a function of the PSD and grain-scale compressibility. Permeability can be related to the void size distribution as (Marshall, 1958):

$$K = \frac{\phi^2 \left[r_1^2 + 3r_2^2 + 5r_3^2 \cdots + (2n-1)r_n^2\right]}{8n^2} \tag{15}$$

where $\phi = (1 - \psi)$ is the current porosity, n is the number of void classes each occupying a volume component ϕ/n of the total porosity, and $r_1 > r_2 > \cdots > r_n$ are the equivalent radii of the voids in the unit area of the section. Fig. 6d offers a glimpse of how the void size distribution (cf. 6a-6c) influences the material permeability. First, as a function of the packing fraction, permeability is not very sensitive to particle compressibility (ν); of course, iit depends on $\bar{\Delta}$, decreasing faster with increasing ν. Second, the *n*G-PSD shows trends that are very similar to the square packing (dotted lines) while the *w*G-PSD trends are close to the *u*-PSD. These are somewhat expected given that the square arrangement and *u*-PSD can be viewed as the limiting cases of *n*G-PSD and *w*G-PSD, respectively (for the same ψ_0). Finally, at $\bar{\psi}_{\text{th}}$, we find $K/K_0 \sim 10^{-2} - 10^{-3}$ where K_0 is the permeability at ψ_0.

5 Summary and Outlook

SGMs occur in nature and technology, from blood clots and starchy foods to bioprinting inks and tissue scaffolds. Their ability to deform, stiffen, heal, and rupture is influenced by how interstitial voids

evolve under deformation. This study reveals that the mechanical stiffening of SGMs arises from a transformation in their void population, marking a second-order rigidity transition that indicates granular confluence. The trends in the void statistics demonstrate that the topology of the void network is geometry dominated and is largely independent of grain compressibility. Particle compressibility has only a mild effect on the qualitative nature of the statistical descriptors, but it primarily influences the strain level at which they appear.

Micromechanical stress fields that evolve during SGM compaction suggest the coexistence of granular-like and continuum-like regions in the vicinity of the threshold packing fraction corresponding to the peak void population. This is somewhat reminiscent of the coexistence of liquid/solid or liquid/vapor phases during phase transitions in materials (Van Wylen et al., 1994). Moreover, at the threshold packing fraction, the macroscopic force-displacement relation exhibits a non-trivial change in the scaling behavior, which suggests a discontinuous transition, which is also referred to as the second-order rigidity transition, in the micromechanical state rather than just a continuous densification.

The emergent void population landscape reported here should extend to three-dimensional (3D) SGMs. What changes is the topology and geometry of the individual voids. In 3D, void spaces may manifest as percolating channels, isolated cavities, and multi-connected structures (Tateno et al., 2025). Their creation and elimination will involve more complex events than in 2D. Capturing this richness may require additional descriptors, but the underlying principle should persist. More broadly, the void-based descriptors introduced here could be integrated into data-driven design pipelines for SGMs that map processing to emergent properties (Verheyen et al., 2023). In particular, tracking, for example using image-based techniques (Vu and Barés, 2019), the peak void population and its associated threshold packing fraction could enrich training datasets with mechanism-informed structure descriptors, improving transferability and interpretability of learned design rules and helping distinguish fragmentation-dominated versus shrinkage-dominated routes to similar macroscopic responses.

Acknowledgements

The authors acknowledge funding support from the National Science Foundation Mechanics of Materials and Structures Program (NSF-MOMS), United States, through the CAREER award CMMI 2042498 (Program Director: Dr. Siddiq Qidwai). The authors acknowledge the use of the Carya cluster and the advanced support from the Research Computing Data Core at the University of Houston, United States, to carry out the research presented here. P.K.P. acknowledges funding support from the University Research Foundation at the University of Pennsylvania.

Appendices

Appendix A Creating Particle Assemblies

For the type of simulation performed in this work, a representative volume (RVE) of size L_0 may comprise a large number of particles (Mutabaruka et al., 2019), which is computationally prohibitive. An alternative is to adopt Statistical Volume Elements (SVEs) of size $l_{\text{sve}} \ll L$, which capture microstructural statistics (Huet, 1982; Ostoja-Starzewski, 2006).

For a given particle size distribution (PSD), we create multiple realizations of RVEs and compare their microstructural characteristics, including the porosity (ϕ_0), total number of particles (N_p), and the mean coordination number ($\langle Z \rangle$). From a typical RVE, we extract a large number ($\mathcal{O} \sim 10^2 - 10^3$) of sub-units of size $l_{\text{cell}} (\ll L_0)$ via random sampling. The microstructural characteristics of these sub-units are assessed as a function of their size ($l_{\text{cell}} \times l_{\text{cell}}$). The results of these analyses allow identifying SVEs, which are defined here as those sub-units whose microstructural characteristics (primarily ϕ_0^{cell}) lies within one standard deviation. For practical purposes, we choose a smaller subset of SVEs whose microstructural characteristics are the closest to that of the parent RVE. The hypothesis is that using these SVEs, one may estimate the overall mechanical behaviors of the RVE reasonably well and within acceptable bounds. The benefit of this approach is the reduction in the computational time, especially considering the fact that multiple SVEs can be simulated simultaneously in a parallel computational environment.

We consider three PSDs: (i) uniform (u-PSD) (5 mm $\leqslant r_0 \leqslant$ 7.5 mm), (ii) narrow Gaussian (nG-PSD) (4 mm $\leqslant r_0 \leqslant$ 6 mm), and (iii) wide Gaussian (wG-PSD) (2 mm $\leqslant r_0 \leqslant$ 8 mm). These PSDs are constructed using the beta cumulative distribution function (Voivret et al., 2007):

$$p = F(x|a,b) = \frac{1}{\beta(a,b)} \int_o^x t^a (1-t)^{b-1} dt, \tag{16}$$

where $a > 0$ and $b > 0$ are parameters that determine the type of PSD and $\beta(a,b) = \Gamma(a)\Gamma(b)/\Gamma(a+b)$ where Γ is the Gamma function.

Figure A1 shows the different statistical volume element (SVE) realizations corresponding to each PSD considered in this work. The boundaries of each SVE are fully periodic.

For a given PSD, the combination of l_{sve} and the number of realizations (N_{sve}) is chosen based on the computational cost and the expected scatter in the data. For instance, we find that for a u-PSD it is computationally less expensive to adopt a larger l_{sve} and a smaller N_{sve} compared to a wG-PSD.

For a given PSD, the results obtained from the simulation of finite element of all SVEs are individually fitted to Eq. (13) and Eq. (14). To do so, we adopt the following approach. Due to the limited number of raw (i.e. from finite element calculations) data points for each SVE, interpolation is performed to obtain values at finer, regular increments as follows. The displacement variable ($\bar{\Delta}$) is increased in small equal increments. Using the `PCHIP` interpolation function in MATLAB®, the corresponding values of ψ, $|\bar{\sigma}|$ and N_v are calculated. For each variable, the average of the interpolated values is computed

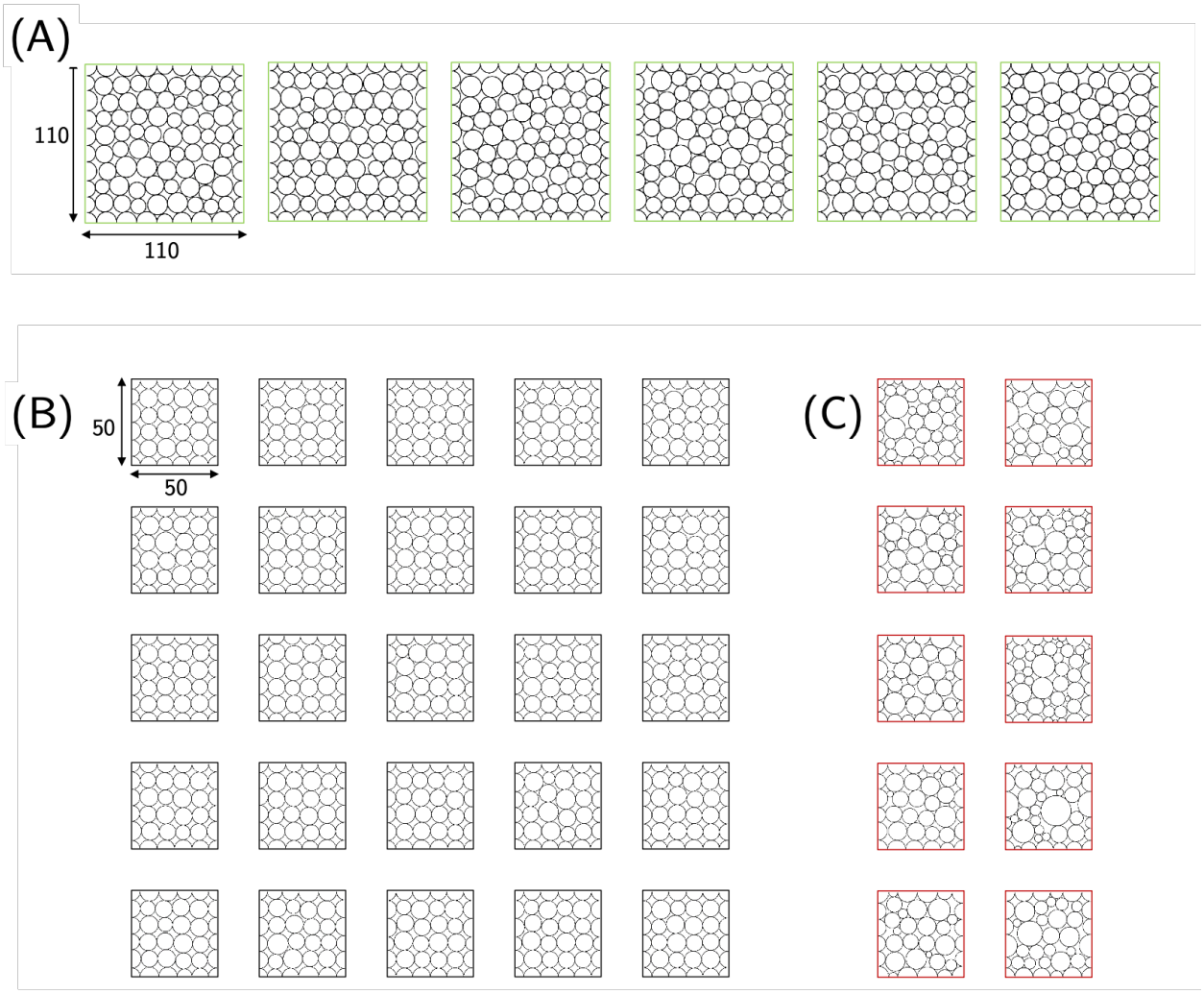

Figure A1 SVE realizations. (A) u-PSD ($l_{\text{sve}} = 110$ mm, $N_{\text{sve}} = 6$) (B) nG-PSD ($l_{\text{sve}} = 50$ mm, $N_{\text{sve}} = 25$), and (C) wG-PSD ($l_{\text{sve}} = 50$ mm, $N_{\text{sve}} = 10$).

over N_{sve} for each $\bar{\Delta}$.

Appendix B Additional Results

Fig. B1 shows the packing evolution profiles in typical granular assemblies that follow wG-PSD and nG-PSD. The corresponding evolution of the packing fraction and normalized stress-displacement behaviors are collated in Figure S3. The resulting fitted parameters for Equations 3 and 4 (Main Text) are given in Tables S2 (wG-PSD) and S3 (nG-PSD). Figure S4 collates the evolution of the probability density functions of the void area, void aspect ratio, and void orientation for these PSDs.

Table B1 Calibrated parameters in Eq. (13) and Eq. (14) for *w*G-PSD (mean $\pm$ s.d.).

ν	α	n	$\bar{\Delta}_{\text{th}}$	S_0	β_0	S_1	β_1
0.495	0.028 ± 0.007	1.02 ± 0.001	0.16 ± 0.003	4.95 ± 0.32	2.01 ± 0.04	342.11 ± 41.62	4.32 ± 0.11
0.34	1.31 ± 0.039	1.77 ± 0.042	0.26 ± 0.004	1.66 ± 0.04	1.68 ± 0.03	4.24 ± 0.09	2.37 ± 0.04
0.20	1.12 ± 0.051	1.55 ± 0.065	0.29 ± 0.001	1.25 ± 0.02	1.56 ± 0.01	2.19 ± 0.09	2.03 ± 0.04

Table B2 Calibrated parameters in Eq. (13) and Eq. (14) for *n*G-PSD (mean $\pm$ s.d.).

ν	α	n	$\bar{\Delta}_{\text{th}}$	S_0	β_0	S_1	β_1
0.495	0.043 ± 0.005	1.02 ± 0.0004	0.19 ± 0.002	7.28 ± 0.43	2.14 ± 0.02	505.79 ± 41.71	4.70 ± 0.05
0.34	1.16 ± 0.024	1.68 ± 0.021	0.32 ± 0.0003	1.79 ± 0.01	1.68 ± 0.005	4.22 ± 0.05	2.43 ± 0.01
0.20	0.98 ± 0.017	1.43 ± 0.017	0.40 ± 0.0004	1.51 ± 0.02	1.66 ± 0.002	2.69 ± 0.04	2.29 ± 0.01

References

Angelini, T.E., Hannezo, E., Trepat, X., Marquez, M., Fredberg, J.J., Weitz, D.A., 2011. Glass-like dynamics of collective cell migration. Proceedings of the National Academy of Sciences 108, 4714–4719.

Barney, C.W., Dougan, C.E., McLeod, K.R., Kazemi-Moridani, A., Zheng, Y., Ye, Z., Tiwari, S., Sacligil, I., Riggleman, R.A., Cai, S., et al., 2020. Cavitation in soft matter. Proceedings of the National Academy of Sciences 117, 9157–9165.

Bhattacharjee, T., Balakrishnan, H., Gopinath, A., Datta, S.S., 2021. Chemotactic migration of bacteria in porous media. Biophysical Journal 120, 3489–3502.

Bhattacharjee, T., Datta, S.S., 2019. Bacterial hopping and trapping in porous media. Nature Communications 10, 2075.

Bosek, M., Ziomkowska, B., Pyskir, J., Wybranowski, T., Pyskir, M., Cyrankiewicz, M., Napiórkowska, M., Durmowicz, M., Kruszewski, S., 2022. Relationship between red blood cell aggregation and dextran molecular mass. Scientific reports 12, 19751.

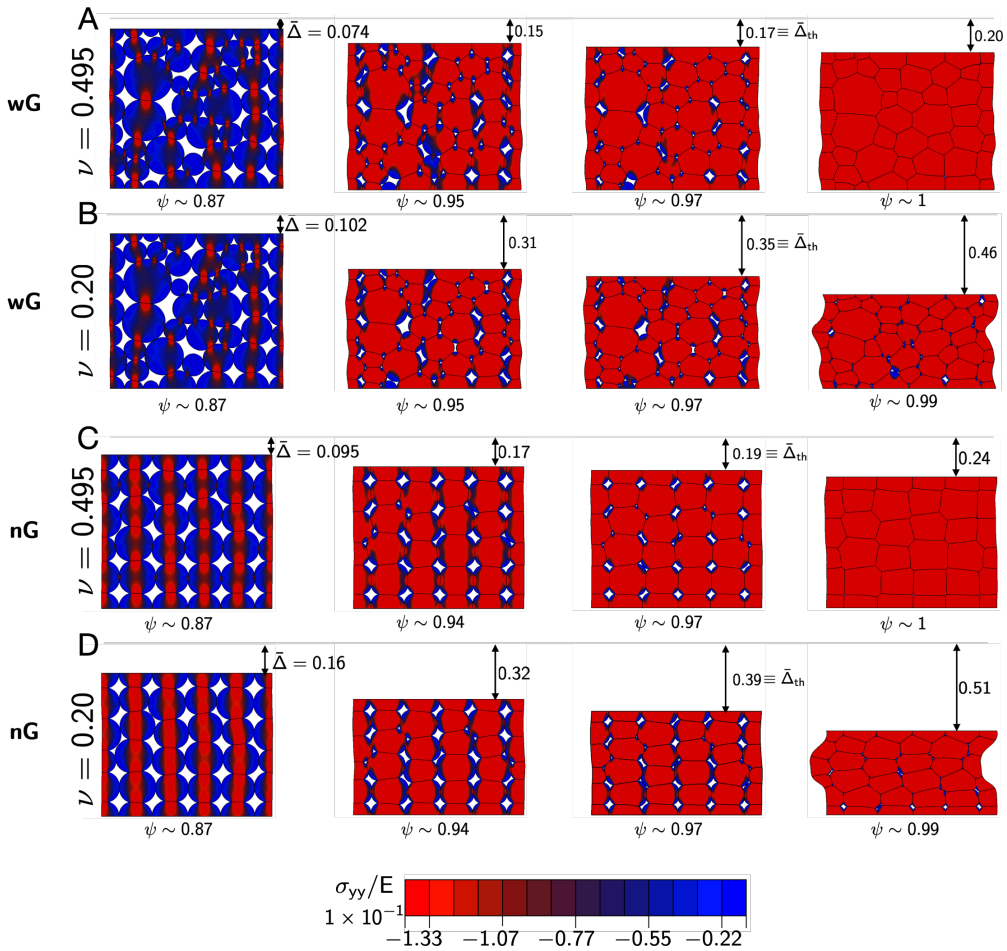

Figure B1 Deformed profiles of a typical granular assemblies for wide Gaussian (*w*G, Panels A and B) and narrow Gaussian (*n*G, Panels C and D). The color contours show the normalized stress (σ_{yy}/E). $\bar{\Delta}_{\rm th}$ is a threshold displacement (Equation 4 in Main Text). Results are shown $\nu = 0.495$ and 0.2. $\nu = 0.34$ shows similar trends.

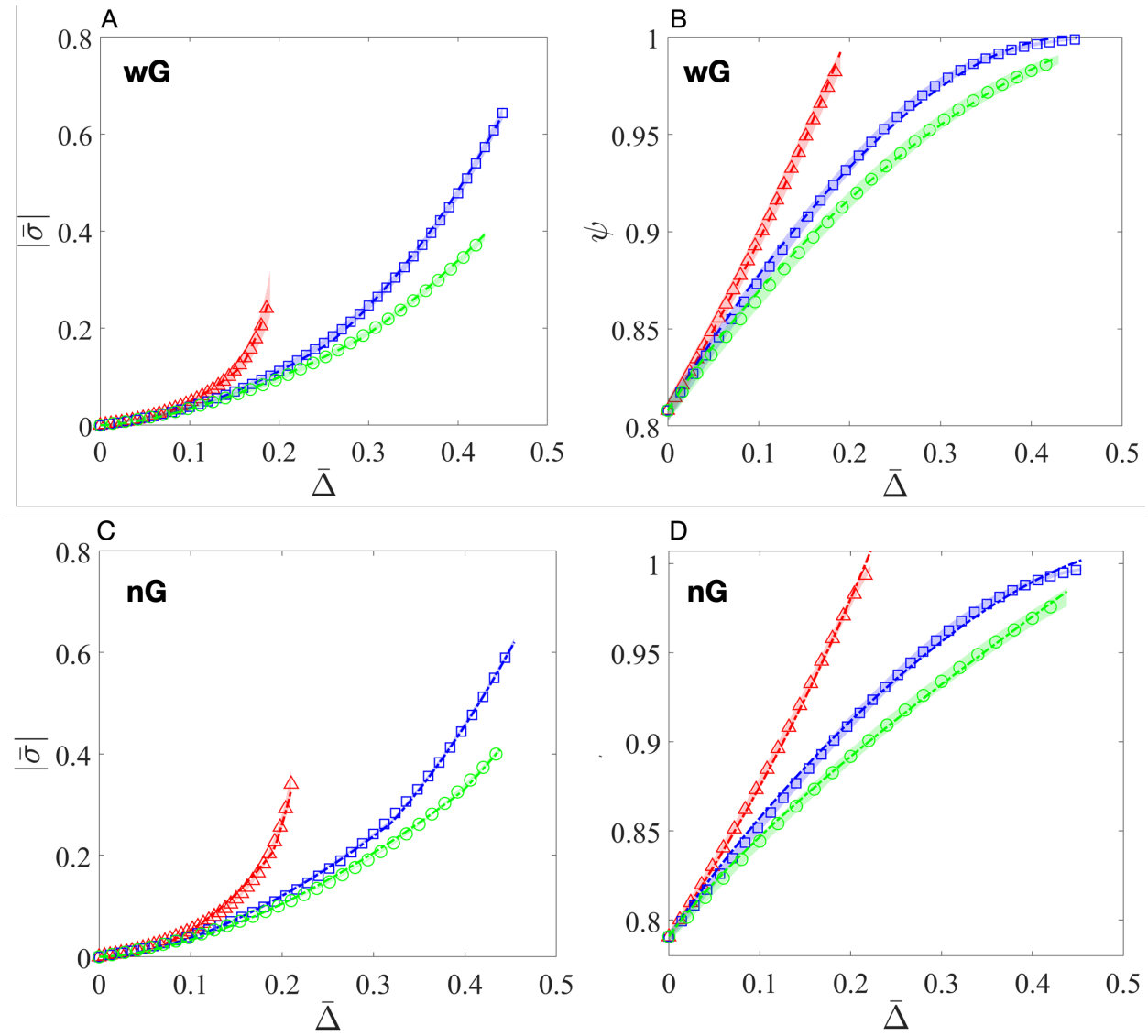

Figure B2 Evolution of normalized overall force, $|\bar{\sigma}|$, (Panels A and C), and overall packing fraction, ψ, (Panels B and D), with normalized displacement, $\bar{\Delta}$. Dashed lines are analytical fits, cf. Equations (3) and (4) in the Main Text. Panels A and B are for wG PSD and Panels C and D are for nG PSD. Red: $\nu = 0.495$, Blue: $\nu = 0.34$, Green: $\nu = 0.2$.

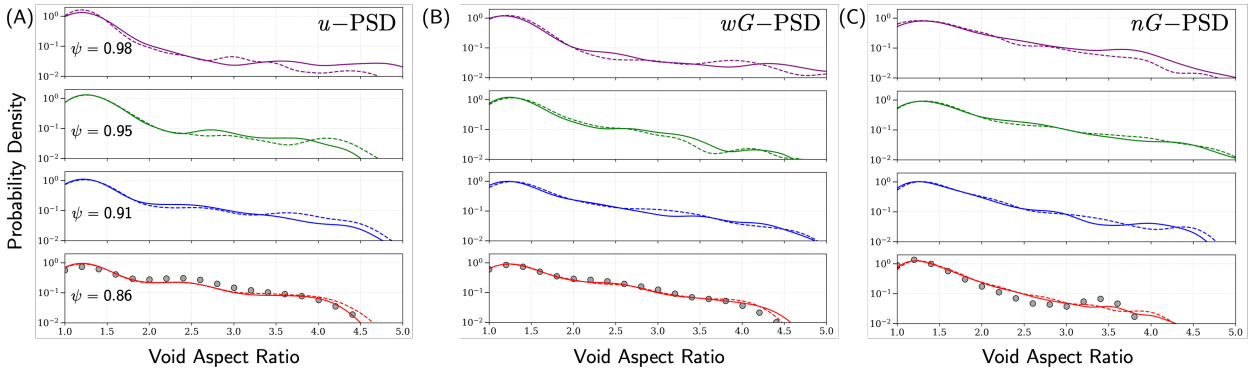

Figure B3 Averaged probability density functions of void aspect ratio at various packing fractions (ψ) for $\nu = 0.495$ (solid lines) and $\nu = 0.2$ (dashed lines). Symbols indicate initial (at ψ_0) values.

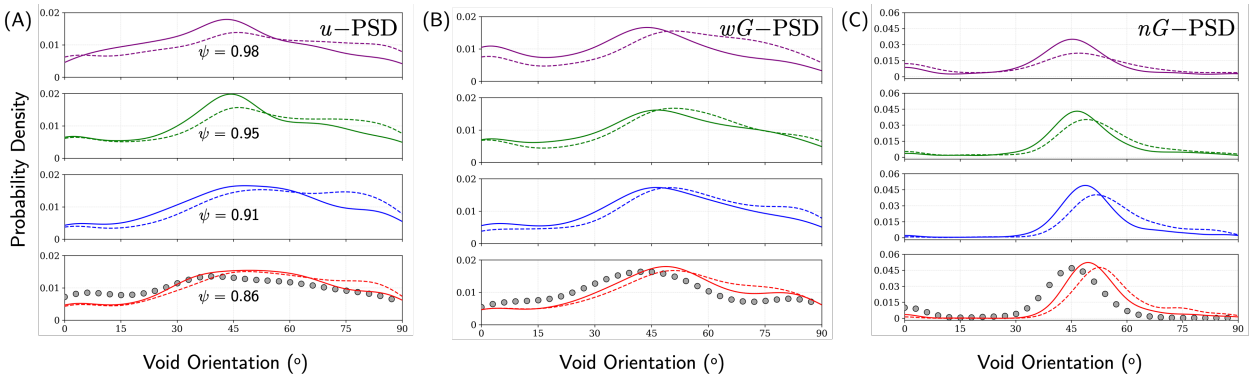

Figure B4 Averaged probability density functions of void orientation relative to the loading (vertical) axis at various packing fractions (ψ) for $\nu = 0.495$ (solid lines) and $\nu = 0.2$ (dashed lines). Symbols indicate initial (at ψ_0) values.

Brodu, N., Dijksman, J.A., Behringer, R.P., 2015. Spanning the scales of granular materials through microscopic force imaging. Nature Communications 6, 1–6.

Cai, G., 2023. Mechanobiology of Jamming: From Collective Migration to Mechanically Tunable Hydrogels. Ph.D. thesis. University of Michigan.

Daly, A.C., 2024. Granular hydrogels in biofabrication: recent advances and future perspectives. Advanced Healthcare Materials 13, 2301388.

Damavandi, O.K., Hagh, V.F., Santangelo, C.D., Manning, M.L., 2022a. Energetic rigidity. i. a unifying theory of mechanical stability. Physical Review E 105, 025003.

Damavandi, O.K., Hagh, V.F., Santangelo, C.D., Manning, M.L., 2022b. Energetic rigidity. ii. applications in examples of biological and underconstrained materials. Physical Review E 105, 025004.

Emiroglu, D.B., Bekcic, A., Dranseike, D., Zhang, X., Zambelli, T., deMello, A.J., Tibbitt, M.W., 2022. Building block properties govern granular hydrogel mechanics through contact deformations. Science Advances 8, eadd8570.

Follmer, S., Leithinger, D., Olwal, A., Cheng, N., Ishii, H., 2012. Jamming user interfaces: programmable particle stiffness and sensing for malleable and shape-changing devices, in: Proceedings of the 25th annual ACM symposium on User interface software and technology, pp. 519–528.

Gao, J., Wang, Y., Dong, Z., Zhou, W., 2018. Structural and mechanical characteristics of bread and their impact on oral processing: A review. International Journal of Food Science and Technology 53, 858–872.

Gent, A., Lindley, P., 1959. Internal rupture of bonded rubber cylinders in tension. Proceedings of the Royal Society of London. Series A. Mathematical and Physical Sciences 249, 195–205.

Griffin, D.R., Weaver, W.M., Scumpia, P.O., Di Carlo, D., Segura, T., 2015. Accelerated wound healing by injectable microporous gel scaffolds assembled from annealed building blocks. Nature materials 14, 737–744.

Hang-Sheng, H., Abeyaratne, R., 1992. Cavitation in elastic and elastic-plastic solids. Journal of the Mechanics and Physics of Solids 40, 571–592.

Holzapfel, G.A., 2002. Nonlinear solid mechanics: a continuum approach for engineering science.

Hommel, J., Coltman, E., Class, H., 2018. Porosity–permeability relations for evolving pore space: a review with a focus on (bio-) geochemically altered porous media. Transport in Porous Media 124, 589–629.

Huang, C., Clayton, J., 1990. Relationships between mechanical properties and microstructure of porous foods: Part i. a review. Engineering and food 1, 352–360.

Huet, C., 1982. Universal conditions for assimilation of a heterogeneous material to an effective continuum. Mechanics Research Communications 9, 165–170.

Jaeger, H.M., Murugan, A., Nagel, S.R., 2024. Training physical matter to matter. Soft Matter 20, 6695–6701.

Jaeger, H.M., Nagel, S.R., Behringer, R.P., 1996. The physics of granular materials. Physics today 49, 32–38.

Karathanos, V., Saravacos, G., 1993. Porosity and pore size distribution of starch materials. Journal of food engineering 18, 259–280.

Lefèvre, V., Ravi-Chandar, K., Lopez-Pamies, O., 2015. Cavitation in rubber: an elastic instability or a fracture phenomenon? International Journal of Fracture 192, 1–23.

Li, H., Sun, J., Herrmann, J.M., 2024. Beyond jamming grippers: granular material in robotics. Advanced Robotics 38, 715–729.

Manning, M.L., 2023. Essay: Collections of deformable particles present exciting challenges for soft matter and biological physics. Physical Review Letters 130, 130002.

Manti, M., Cacucciolo, V., Cianchetti, M., 2016. Stiffening in soft robotics: A review of the state of the art. IEEE Robotics & Automation Magazine 23, 93–106.

Marshall, T., 1958. A relation between permeability and size distribution of pores. Journal of soil science 9, 1–8.

Mason, T., Bibette, J., Weitz, D., 1995. Elasticity of compressed emulsions. Physical review letters 75, 2051.

Monfared, S., Ravichandran, G., Andrade, J., Doostmohammadi, A., 2023. Mechanical basis and topological routes to cell elimination. Elife 12, e82435.

Mukhopadhyay, S., Peixinho, J., 2011. Packings of deformable spheres. Physical Review E—Statistical, Nonlinear, and Soft Matter Physics 84, 011302.

Murray, J.D., 2007. Mathematical biology: I. An introduction. volume 17. Springer Science & Business Media.

Mutabaruka, P., Taiebat, M., Pellenq, R.J.M., Radjai, F., 2019. Effects of size polydispersity on random close-packed configurations of spherical particles. Physical review E 100, 042906.

Noell, P.J., Sills, R.B., Benzerga, A.A., Boyce, B.L., 2023. Void nucleation during ductile rupture of metals: A review. Progress in Materials Science 135, 101085.

Ostoja-Starzewski, M., 2006. Material spatial randomness: From statistical to representative volume element. Probabilistic Engineering Mechanics 21, 112–132.

Peshkova, A.D., Rednikova, E.K., Khismatullin, R.R., Kim, O.V., Muzykantov, V.R., Purohit, P.K., Litvinov, R.I., Weisel, J.W., 2025. Red blood cell aggregation within a blood clot causes platelet-independent clot shrinkage. Blood Advances , bloodadvances–2024015533.

Poincloux, S., Takeuchi, K.A., 2024. Rigidity transition of a highly compressible granular medium. Proceedings of the National Academy of Sciences 121, e2408706121.

Prakash, V.N., Bull, M.S., Prakash, M., 2021. Motility-induced fracture reveals a ductile-to-brittle crossover in a simple animal's epithelia. Nature Physics 17, 504–511.

Qazi, T.H., Burdick, J.A., 2021. Granular hydrogels for endogenous tissue repair. Biomaterials and Biosystems 1, 100008.

Rahman, M.S., 2001. Toward prediction of porosity in foods during drying: A brief review. Drying Technology 19, 1–13.

Riley, L., Schirmer, L., Segura, T., 2019. Granular hydrogels: emergent properties of jammed hydrogel microparticles and their applications in tissue repair and regeneration. Current Opinion in Biotechnology 60, 1–8.

Risman, R.A., Abdelhamid, A., Weisel, J.W., Bannish, B.E., Tutwiler, V., 2022. Effects of clot contraction on clot degradation: a mathematical and experimental approach. Biophysical Journal 121, 3271–3285.

Selvaraju, S., Joshi, S.P., Karanjgaokar, N., 2024. Viscoelastic mechanics of two-dimensional granular lattices. Journal of the Mechanics and Physics of Solids 185, 105574.

Tateno, M., Wang, Y., Tanaka, H., 2025. Void connectivity and criticality in the compression-induced gel-to-glass transition of short-range attractive colloids. Physical Review Letters 134, 048201.

Truong, N.F., Kurt, E., Tahmizyan, S., Lesher-Perez, S.C., Chen, M., Darling, N.J., Xi, W., Segura, T., 2019. Microporous annealed particle hydrogel stiffness, void space size, and adhesion properties impact cell proliferation, cell spreading, and gene transfer. Acta Biomaterialia 94, 160–172.

Tutwiler, V., Mukhitov, A.R., Peshkova, A.D., Le Minh, G., Khismatullin, R., Vicksman, J., Nagaswami, C., Litvinov, R.I., Weisel, J.W., 2018. Shape changes of erythrocytes during blood clot contraction and the structure of polyhedrocytes. Scientific reports 8, 17907.

Tutwiler, V., Singh, J., Litvinov, R.I., Bassani, J.L., Purohit, P.K., Weisel, J.W., 2020. Rupture of blood clots: Mechanics and pathophysiology. Science advances 6, eabc0496.

Van Dalen, G., Nootenboom, P., Van Vliet, L.J., Voortman, L., Esveld, E., 2007. 3-d imaging, analysis and modelling of porous cereal products using x-ray microtomography. Image analysis and stereology 26, 169–177.

Van Wylen, G., Sonntag, R., Borgnakke, C., 1994. Fundamentals of Classical Thermodynamics. Wiley.

Varner, H., Sugerman, G.P., Rausch, M.K., Cohen, T., 2023. Elasticity of whole blood clots measured via volume controlled cavity expansion. journal of the mechanical behavior of biomedical materials 143, 105901.

Verheyen, C.A., Uzel, S.G., Kurum, A., Roche, E.T., Lewis, J.A., 2023. Integrated data-driven modeling and experimental optimization of granular hydrogel matrices. Matter 6, 1015–1036.

Voivret, C., Radjaï, F., Delenne, J.Y., El Youssoufi, M.S., 2007. Space-filling properties of polydisperse granular media. Physical Review E 76, 021301.

Vu, T.L., Barés, J., 2019. Soft-grain compression: Beyond the jamming point. Physical Review E 100, 042907.

Vu, T.L., Barés, J., Mora, S., Nezamabadi, S., 2019. Numerical simulations of the compaction of assemblies of rubberlike particles: A quantitative comparison with experiments. Physical Review E 99, 062903.

Vu, T.L., Nezamabadi, S., Mora, S., 2021. Effects of particle compressibility on structural and mechanical properties of compressed soft granular materials. Journal of the Mechanics and Physics of Solids 146, 104201.

Weaire, D., Aste, T., 2008. The pursuit of perfect packing. CRC Press.

Widener, A.E., Roberts, A., Phelps, E.A., 2024. Granular hydrogels for harnessing the immune response. Advanced Healthcare Materials 13, 2303005.

Yuk, H., Wu, J., Sarrafian, T.L., Mao, X., Varela, C.E., Roche, E.T., Griffiths, L.G., Nabzdyk, C.S., Zhao, X., 2021. Rapid and coagulation-independent haemostatic sealing by a paste inspired by barnacle glue. Nature Biomedical Engineering 5, 1131–1142.